The Virtual Parkinsonian Patient

Marianna Angiolelli, Damien Depannemaecker, Hasnae Agouram, Jean Regis, Romain Carron, Marmaduke Woodman, Letizia Chiodo, Paul Triebkorn, Abolfazl Ziaeemehr, Meysam Hashemi, et al.

The Virtual Parkinsonian Patient

Marianna Angiolelli[1,2], Damien Depannemaecker[1], Hasnae Agouram[3], Jean Régis[4], Romain Carron[1,5], Marmaduke Woodman[1], Letizia Chiodo[2], Paul Triebkorn[1], Abolfazl Ziaeemehr[1], Meysam Hashemi[1], Alexandre Eusebio[3,6] , Viktor Jirsa[1], Pierpaolo Sorrentino[1,7]

1. Aix-Marseille Univ, INSERM, INS, Institut de Neurosciences des Systèmes, Marseille, France
2. Department of Engineering, Università Campus Bio-Medico di Roma, Rome, Italy
3. Aix Marseille Univ, CNRS, INT, Institut de Neurosciences de la Timone, Marseille, France
4. Aix Marseille Univ, UMR INSERM 1106, Dept of Functional Neurosurgery, Marseille France
5. Medico-surgical Unit Epileptology, Functional and Stereotactic Neurosurgery, Timone University Hospital, Marseille, France
6. APHM, Hôpitaux Universitaires de Marseille, Hôpital de la Timone Department of Neurology and Movement disorders, France
7. Department of Biomedical Sciences, University of Sassari, Sassari, Italy

* corresponding author: Pierpaolo Sorrentino. Email: pierpaolo.sorrentino@univ-amu.fr

Abstract

Parkinson's disease is one of the most diffuse neurodegenerative diseases. While the aetiology of Parkinson's disease remains elusive, the degeneration of the dopamine - producing nigrostriatal neurons, along with the accumulation of alpha-synuclein, are pathophysiological hallmarks. The impairment of motor functions, a consequence of the involvement of the thalamic-frontal loop, dominates the overt clinical picture. However, more recent findings clarified that the symptoms are more widespread, and cognitive and/or behavioral dysfunctions are also common. Accordingly, neuroimaging studies show that, even in early disease, structural and functional alterations are not confined to the motor areas. This suggests that the effects of the nigro-striatal neurodegeneration are not restricted to the motor areas alone but, rather, they modify the behavior of the brain on a large scale. Understanding how the local degeneration of dopaminergic neurons affects the whole brain dynamics remains an open question.

The purpose of this study is to understand how the ability of the nigrostriatal pathways to support a dopaminergic stimulation affects the brain as a whole. To this end, we leverage simultaneous recordings from EEG and deep electrodes placed near the subthalamic nuclei (STN) from 10 Parkinsonian patients, acquired both before and after administration of L-Dopa. We used the topography of the spreading of aperiodic waves over a large scale (i.e. neuronal avalanches), utilizing the recently described avalanche transition matrix (ATM), to characterize the brain dynamics. To simulate the effect of L-Dopa in silico, we deployed a mechanistic neural-mass model derived from the adaptive quadratic integrate-and-fire model (aQIF) of individual neurons that has been extended to include dopamine concentration as a variable. Each parcelled brain region is equipped with a neural mass and then coupled according to the empirical connectomes, where connections can be either excitatory, inhibitory, or dopaminergic. Then, the whole-brain dynamics have been simulated for different configurations, i.e., for different dopaminergic tones. This way, we obtained a numerical prediction of the expected dynamics (in terms of properties of the ATMs), as observed in the deep electrodes and the EEG, given different dopaminergic tones. Then, in a Bayesian set-up, we used a class of deep neural networks to "invert" the model and infer the most likely dopaminergic tone given the empirically observed dynamics. For all ten patients, we correctly inferred that the dopaminergic tone was higher given the dynamics observed after administration of L-Dopa, and lower before. In other words, we could distinguish and quantify the dopaminergic tone from the electrophysiological data if the subjects had orally taken L-Dopa. This was achieved by integrating the background (anatomical and dynamical) knowledge into model prediction about the physiology of dopamine (as opposed to training a classifier to distinguish empirical data). Finally, we carried out a diagnostic for the validation of the model, as well as a further description of the simulated dopamine dynamics.

Introduction

Parkinson's disease (PD) is the second-most common neurodegenerative disorder, imposing a significant socio-economic burden [1]. The pathophysiology is characterized by the degeneration of dopaminergic neurons in the substantia nigra, and the consequent depletion of dopamine in the nigrostriatal pathways [2]. Such alterations disrupt normal activity patterns, affecting brain dynamics on a large scale [3]. Accordingly, changes in the cortical dynamics are more predictive of clinical symptoms as compared to basal ganglia dynamics[4]. In turn, the symptoms are not restricted to motor abilities but, rather, involve multiple domains[5]. In line with this, structural Magnetic Resonance Imaging (MRI) has shown that the areas impacted by PD are more extensive than once believed[6]. Functional MRI (fMRI) has revealed dysfunctions in the cortico-striatal networks, with these disruptions extending to various other brain regions[7]. A magnetoencephalography (MEG) study demonstrated global changes in fast brain dynamics in PD, showing stereotyped brain dynamics as compared to controls, with the flexibility of the dynamics shrinking proportionally to clinical impairment [8].
How does the degeneration primarily occurring in the nigro-striatal pathways impact the whole brain? More specifically, how does the inability to sustain appropriate dopaminergic tone in the nigro-striatal pathways affect activities elsewhere?

We aim to elucidate how effective dopaminergic tone influences large-scale brain dynamics, drawing from empirical data[9] and utilizing large-scale mechanistic whole-brain models[10]. To accomplish this, we leverage data acquired from Parkinsonian patients both before (OFF state) and after (ON state) the administration of treatment with L-Dopa. Each patient has six EEG electrodes placed above the motor areas and two deep leads (four contacts each) near the left and right subthalamic nuclei[9]. We use the recently described avalanche transition matrix (ATM) to capture the brain dynamics[11]. Focusing on aperiodic large-scale bursts of activities (i.e. neuronal avalanches), the ATMs capture the probability of large-scale activities consecutively propagating across any two regions. The transition probabilities are altered in neurodegenerative diseases [12,13], and by the presence of a task [14]. This way, we have quantified the coordination of the activities recorded in the electrodes implanted in patients both in the ON and the OFF states.

In parallel, we deployed a mechanistic model, known as the *Dody (Dopamine Dynamics) model,* that is derived from the adaptive quadratic integrate-and-fire (aQIF) model of individual neurons[10]. While originally designed for a single population of neurons, we have now coupled the model's equations according to three different connectivity matrices, representing excitatory, inhibitory, and dopaminergic connections, respectively. We wish to study a variable of interest that represents the dopaminergic tone, and its effect on the whole-brain dynamics. This variable represents the ability of the nigro-stratal pathways to effectively project their activities to the rest of the brain (that is, to respond to a dopamine load effectively). The evolution of local dopamine is captured by a dedicated differential equation, with one term corresponding to the increase of concentration due to dopaminergic projection and a second term capturing the reuptake mechanisms through Michaelis-Menten kinetics[15,16], which describes the dynamics of dopamine concentration. In turn, the dopamine concentration impacts the model's dynamics, as it is included in the mean-field equation of the membrane potential. This effect is mediated by the connectome (which we assume to be constant in the On and Off state) [17], and a free parameter, which is our parameter of interest to estimate, as it provides insights into the effectiveness of the stimulation. We have then projected out the simulated activities to virtual electrodes, thence providing a prediction that can be straightforwardly compared to the empirical data. In simpler terms, the model predicts how changes in dopaminergic tone affect large-scale brain dynamics.

To quantify the uncertainty of our prediction, we use a Bayesian framework implemented with advanced probabilistic machine learning techniques, called simulation-based inference (SBI[18]) to efficiently invert the model[19]. In other words, we infer the posterior distribution of dopaminergic tone given the (low-dimensional data features of) empirical ATM patients. If our prediction is correct, we expect that the model would predict higher dopaminergic tone given the data acquired in the ON state, and lower when inferring the dopaminergic tone starting from data acquired during the OFF state. We test this in each participant. The overall pipeline of this approach is shown in Fig. 1.

In this process, we must consider some key points to achieve our goal. Firstly, it is essential to understand which brain data features indicate optimal brain activity to replicate individual dynamics in silico and to predict the effects of different dopaminergic tones on individual patients. This needs to be sufficiently informative about the brain dynamics yet low-dimensional for the efficiency of SBI.

Results

Dody Model: generation of dopamine-driven dynamics

Starting from the model described in this work[10], where dopamine has been included, we modify the connection terms, expanding from a single-node framework to whole-brain according to three distinct layers that simulate different types of neuronal connections: excitatory, inhibitory, and dopaminergic. Each structural connection can be part of one layer (that is, it is either excitatory, inhibitory, or dopaminergic). A connection scaling factor, either w_{dopa}, w_{inh}, or w_{exc}, modulates each layer. In other words, if a connection is excitatory, it will be scaled by w_{exc}, inhibitory by w_{inh}, and dopaminergic by w_{dopa}. The connections are shown in Fig. 2 A. The types of connections are not merged because they play different roles in the brain. This is encapsulated mathematically as each type of connection enters the equation differently, simulating different action mechanisms.

A parameter exploration is carried out to observe the qualitative changes in the system dynamics. To understand the dynamics of the model we used previous results at the single node level[10]. Then we focus at the network level to understand how the interplay between the three layers of connectivity (excitatory, inhibitory, and dopaminergic) would affect the overall dynamics. For these reasons, we systematically vary the parameters (w_{dopa}, w_{inh}, w_{exc}) to shift the system into a different regime. Thus, we set these values within the range that would let the whole-brain model exhibit a rich dynamical repertoire, as observed in brain recordings. In other words, we aim to simulate emerging dynamics at the whole-brain level.

Fig. 2 provides an overview of the dynamics generated by the Dody model. Specifically, after establishing fixed values for w_{inh} and w_{exc} (as our focus is to simulate the effects of altered dopaminergic tone, see Fig. 2, panel A), we explore how changes in w_{dopa} influence the system. This simulation aims at mimicking scenarios when patients are being administered L-Dopa. Fig 2 panel B exemplifies the part of the parameter space that was explored. The global dynamics become richer for higher dopaminergic tones, as more regions are recruited across the brain than for lower dopaminergic tones. Despite only modifying the term related to dopaminergic connections, a qualitative change in dynamics is observed across the whole brain, in particular, Fig. 2, first row of panel C, shows the phase planes of the fast variables, namely firing rate and voltage, as a function of increasing w_{dopa} (left to right. The second row of the same panel shows how the increasing of dopaminergic tone impacts the Subthalamic Nuclei. One can observe that the system displays large oscillations for low values of dopaminergic tone, which diminish as the dopaminergic tone increases. The corresponding time series, (panel D, firing rate at the top, voltage at the bottom) show that, for low levels of dopaminergic tone, the activities across the brain are highly coordinated, with large synchronous oscillations recruiting all regions. Conversely, for high dopaminergic tones (at equal levels of noise) the system shows less-stereotyped activities. In the next step, we project the simulated activities to the sensor space using a lead field matrix. This is a necessary step, going from the simulated source activities to time-series that can be directly compared to the empirical data. Specifically, we projected out the source activities to the EEG channels located above the motor-sensory areas bilaterally, that is F3, C3, F4, C4, Fz, and Cz. In short, the sensor-level signals are understood as a weighted linear superposition of all the source-level activities. As per the subthalamic nuclei (STN), the simulated voltages have been compared directly to the lead field potential recorded by deep electrodes placed in the STNs bilaterally. Figure 3, panel B reports the time series of the simulated voltages in OFF (above, signified by the small pills) and in ON (below, signified by the larger pills). Going from the bottom to the top, the first six time series correspond to the simulated EEG signals (i.e. after the projection via the lead field), and the remaining two time series correspond to the activities of the subthalamic nuclei (see methods for details). To characterize the spatio-temporal dynamics over a large scale, we utilize avalanche transition matrices, which track the spreading of nonlinear bursts. First, the z-scored signals have been binarized, and set to 1 for z>2, and to 0 otherwise. This way, the bursts of activations were identified. Then, for each burst, the probability of two channels being consecutively recruited is estimated, obtaining an N x N matrix, with N the number of channelss. Then, these matrices are averaged, element-wise, over the number of bursts, which yield one ATM per dopaminergic tone (i.e. the values of w_{dopa}). Fig. 3, panel B, shows the ATMs for low (top) and high (bottom) dopaminergic tone.

To provide an extensive characterization of the whole-brain dynamics, we extract features from both the z-scored data and the ATMs. We compute from the normalized time series the kurtosis of each signal (obtaining a vector of length N), and the variance of the pairwise differences of entropy over all the couple of signals. We compute from the ATMs the sum, arithmetic mean, skewness, and kurtosis. Furthermore, we also compute from the ATMs the Coefficient of Variation, defined as the ratio of the standard deviation to the mean, and its inverse. Finally, the Frobenius norm and the entropy (H) of the matrix, defined as $H=-\sum(p\log2(p))$, where $\log2(p)$ is the base-2 logarithm of the probability distribution of signals, are computed. To learn a function to map from the dopaminergic tone to the expected dynamical features, we carry out many random brain simulations, each with a w_{dopa} drawn from a uniform distribution (within the ranges explored in the parameter exploration). For each simulation, the resulting features were stored (with the dimension of 10. With the budget of 3000 simulation, we trained Masked Autoregressive Flows[20] to estimate the posterior distribution. Figure 3, panel C shows a selection of such features as a function of the dopaminergic tone (w_{dopa}). In each plot, each dot refers to the observed feature at the corresponding value of w_{dopa}. The scatter plots show a distinct relationship between the dopaminergic tone and the generated large-scale dynamics. Then, we perform the Bayesian model inversion starting from the empirical data, recorded in each patient's ON and OFF state. That is, based on the relationships that we found by simulating data features as a function of w_{dopa}, and we estimate the most likely dopaminergic tone given a set of data features.

To estimate the posterior distributions of w_{dopa}, we apply simulation-based inference (SBI) for efficient Bayesian model inversion [21,22]. We utilize a class of machine learning generative model for probability density estimation called Masked Autoregressive Flow (MAF) [23], trained with 3000 random model simulations, each with a value of w_{dopa} drawn from a uniform distribution [24]. The values of w_{dopa} and the features of the resulting dynamics are fed to the MAF, which learns an invertible function that maps the dopaminergic tone to the expected data features [18]. Then, the inversion process yields the posterior distribution of the most likely w_{dopa} values (i.e. the conditional probability of w_{dopa} given low-dimensional data features).

Firstly, we test for the accuracy and reliability of the inversion using synthetic data. To this end, after training the MAF, we sampled from posterior distribution of dopaminergic tone for different model configurations (i.e. w_{dopa}). As shown in Fig. 3, panel D, to the left, the inferred w_{dopa} (5 random values for example) matched the ground truth. The plot illustrates how the estimated values, represented as $\tilde{w}_{dopa}$, are interpolated by a linear regression line, which closely follows the dashed black line defined by the equation y=x as a perfect fit, indicating that the inferred parameters correspond exactly to the ground truth values. On the right there is a zoom on three of these values. Fig. 3, panel D, to the right, displays the distribution of posterior z-scores and posterior shrinkage within the Bayesian distribution (see section Methods), highlighting typical pathologies of Bayesian inference. The estimated posterior distributions for different configurations exhibit high posterior shrinkage and low posterior z-scores, positioning them in the ideal Bayesian estimation.
We then characterize the empirically recorded dynamics in the ON and OFF states according to the same data features, to infer the dopaminergic tone from the empirical data.

Empirical differences between patients with and without L-Dopa treatment and model inversion

While analyzing empirical data, the primary objective is to differentiate the dynamics recorded during the ON state from the one recorded during the OFF state[9]. We compute, in each patient, the avalanche transition matrices from the EEG and LFP recordings acquired either during the OFF condition or the ON condition. We follow the aforementioned procedure, where each signal (either EEG or LFP) is z-scored, thresholded, and the ATMs computed. In summary, each subject has the time series recorded during the ON and OFF states, and two corresponding ATMs, as shown in Fig. 4, panel A. One can see that, in the on-condition, in each subject, the ATMs contain higher transition probabilities. The ATMs in the ON and the OFF state are reported, as an example, for one patient, in (Fig. 4 panel A). However, the transition probabilities are globally higher in the ON state in every subject, as shown in Fig. 4 panel A, top left. The other plots in panel B show the difference between the ON and the OFF states in every subject for various features. Finally, the empirical data features (during the ON or the OFF state) are fed to the trained MAF that yields the posterior distribution for the ON and

the OFF states. Fig.5, panel A shows, for each patient, the posterior distribution for w_{dopa} given the data recorded during the OFF state (orange) and the ON state (blue). For all patients, the inversion infers a lower dopaminergic tone when starting from data acquired during the OFF state and conversely, a higher dopaminergic tone when starting from data from the ON state. We regard the ON and OFF states as ground truths since L-Dopa had been orally given to all the participants before the ON-state recording, likely changing the effectiveness of the dopaminergic stimulation.

We use the Wasserstein distance to quantify the differences between the distributions of the estimated w_{dopa} in the two conditions (Fig. 5 panel B). Furthermore, we report the shrinkage of the posterior distributions as compared to the priors (that is, the reduction of uncertainty about the "true" w_{dopa} provided by the empirical data, or the level of information in the posterior updated from prior). The shrinkage for all the distributions are close to 1, indicating that there is a significant reduction of the uncertainty of the dopaminergic tone. Moreover, the Wasserstein distance between the posteriors inferred from the ON and the OFF states is always greater than 0, implying that the two distributions are significantly different.

Comparison of the synthetic and the empirical dynamics

Finally, we aim to compare the dynamics generated by the numerical simulations in either the ON or the OFF states and the corresponding observed dynamics. To provide a comprehensive representation of the dynamics generated by the model, and to avoid tautologies, we include both the data features used for model inversion and additional features not used in the inversion process. Specifically, we incorporate the standard deviation, the median, the maximum eigenvalue, the trace, and the ratio of the mean to the kurtosis of the ATM matrix for each w_{dopa} value. To test the ability of the model to generate realistic differences in the dynamics in the ON and OFF states across the whole set of these metrics we compute, for each patient, the Spearman's correlation between the observed and the simulated differences. The simulated differences were defined as the differences between the data features generated by re-simulating the model using the most likely w_{dopa} in the ON and the OFF states (called out-of-sample posterior predictive check). For the synthetic data, we report average values over 30 simulations, where the starting conditions (and the dynamical noise) are different. Fig. 6, Panel A, shows that the simulated and empirical differences (between the ON and OFF states) across metrics are directly related in all subjects. This result points out the capability of the model to generate realistic variations in a number of dynamical features, effectively mirroring the empirical data. Furthermore, we test the consistency of the performance of the metrics in the synthetic and the empirical data. In other words, we compute the Spearman's correlation between the difference of the features in the ON states (synthetic and empirical) and the differences for the same features in the OFF states (synthetic and empirical) . In other words, the metrics differ from each other with respect to the magnitude of the distance between the ON and the OFF states. However, there is a clear relationship across metrics with respect to the magnitude of these differences. Simply put, if a particular metric shows a small difference between the values estimated in the synthetic data and in the empirical data in the ON state, then this metric will also show a small difference in the OFF state. Conversely, a metric that estimates a large difference in the ON state will behave similarly in the OFF state. This is to say that the magnitude of the difference depends on the metrics at hand, and it is not justified by noise alone. In Fig. 6, Panel B, we report the differences for 4 subjects, and in the Supplementary materials S3 we report the data for all the participants.

We now consider the clinical improvement observed in patients in the ON and the OFF condition, as measured by the Unified Parkinson's Disease Rating Scale (UPDRS), a comprehensive tool used to quantify the severity of PD symptoms. Specifically, the UPDRS Part III (UPDRS-III) focuses on motor examination and is pivotal in assessing the motor function of PD patients. For each patient, the differences of the UPDRS-III in the ON and OFF conditions are computed and correlated to the difference of the mean value of the simulated ATM matrices in the ON and the OFF states (r= 0,60). This result is to be confirmed with a larger sample, since for one patient the clinical data are missing, and we removed one outlier (See methods for details). However, the preliminary data suggest that the generated feature might hold significance in terms of behavioral output.

As a last analysis, we explore the time series of the dopamine concentrations [Dp]_e for different w_{dopa} values, as shown in the figure S4 of Supplementary materials, and the distribution of the [Dp]_averaged over the STN, the Putamen and the Caudate. By observing the dopamine concentration values for individual regions, we note

distinct behaviors and values that each region reaches in a steady state, depending on whether the starting point is in the ON or OFF state. In this way, the figure illustrates the variability and statistical characteristics of the brain activity under the two conditions for each patient, potentially highlighting differences due to the presence or absence of a drug or therapeutic intervention.

Discussion

In this paper, we set out to build a mechanistic model to infer the dopaminergic tone in individual patients acquired with a combination of EEG and intracranial electrodes before and after the administration of L-Dopa. Simulating data using the model, and then inverting it using deep neural networks, we successfully infer lower dopaminergic tone starting from data acquired before and after the intake of L-Dopa.

The Bayesian model inversion is based on a mechanistic model while allowing us to integrate the background knowledge in the form of prior distribution, and reveal the causal mechanism(s) at microscopic level from macroscopic measurements. That is, the identification of the state of the patient (either ON or OFF, is not based directly by learning statistical features but, rather, on the inference of a biologically plausible mechanism [25]. In contrast, phenomenological models focus on describing observable phenomena without necessarily linking them to the underlying biological mechanisms. They are often used to fit and predict data patterns based on empirical observations, without providing insights into the causal mechanisms.

The *Dody model* is a neural mass model derived from the adaptive quadratic integrate-and-fire model (aQIF) which has several differences with previous models that have been used thus far[10]. Adapted from a mean-field derivation[26], the neural mass has been modified to include an additional variable capturing the local dopamine concentration. As a consequence, each connection affects the neural masses differently, according to its nature, that is dopaminergic, excitatory, or inhibitory. In other words, the neural masses are then coupled according to the empirical connectome, where connections can be either excitatory, inhibitory, or dopaminergic. This model encapsulates a wealth of well-established information about the specific role of each connection (i.e. the directionality and whether it is inhibitory, dopaminergic, or excitatory), which has been typically disregarded in large-scale models thus far [27,28]. To do so, each tract, as measured from the tractography, is considered with directionality and with a specific functional role (as an example, the tract from i to j might be inhibitory while the tract j to i excitatory).
The individual structural connectomes were not available. Thence, unlike typical virtualization pipelines, we built one generic model that was used to perform inference on each patient. As explained, the coupling was done according to a connectome computed as the edge-wise average of 10 healthy subjects extracted from the Human Connectome project[29].
This particular design speaks to the validity and the generalizability of our pipeline. In fact, in this work we aim to capture the functional deficit of the nigro-striatal pathways which is the *primum movens* in each Parkinsonian patient [30]. Accordingly, our model simulates the expected changes in terms of large-scale brain dynamics as a function of the nigro-striatal stimulation. In the model inversion, the model was estimated against data from each of the 10 patients, and the inversion is successful in each as shown by the shrinkage of the posteriors. This might be interpreted as the fact that the model, and the features used for the inversion, are valid for the effect that L-Dopa exerts on the dynamics of patients in general. This mechanistic explanation constitutes a hypothesis of the effect of L-Dopa on the corresponding large-scale activities. Based on this evidence, our model provides a prediction that is not yet personalized, but rather reproduces a generic set of features for each subject across the cohorts[31]. However, the model successfully distinguishes the ON and OFF conditions in each patient individually. In other words, how do changes in the ability of the nigro-striatal pathways to uptake L-Dopa, process it, and release dopamine affect brain dynamics, as observed from a change in data features from large-scale data?

With respect to the data features that we selected, we focused on the topology of the spread of large-scale aperiodic bursts [11,32]. This approach is complementary to most traditional methods, which focus on the presence of synchronization or the dynamics of local bursts, typically in the beta band (13-30 Hz) [33–37] [38]. In addition to calculating various features from the EEG signals, we utilized the recently described ATMs to capture the spatio-temporal spreading of each such perturbation [11]. Of note, we found that the ATMs were informative about the large-scale dynamics yet low-dimensional, as we were able to accurately estimate the posterior distribution from these features (e.g. the mean, the kurtosis, etc), which were consistently different between ON and OFF at

the individual level. The experimental setting, contrasting each individual before and after the assumptions of L-Dopa, allowed us to establish a causal relationship between the administration of L-Dopa and the changes in the dynamics over the large scale. Nevertheless, revealing a true causal mechanism requires considering inference on multiple causal factors and then comparison by measuring the model evidence, which requires thorough investigation and has not yet been demonstrated using SBI. Furthermore, we demonstrated the possibility to define cross-modality connectivity matrices, since some of the transition probabilities were computed starting from deep electrodes and going to EEG electrodes, or vice-versa.

We use Bayesian model inversion to answer the question, "What is the most probable intensity of the nigro-striatal pharmacological stimulation that generates the features observed from the empirical data?" In our scenario, we wanted to simulate the effects of varying levels of dopaminergic tone (represented by different values of w_{dopa}) on the data features. This allows us to estimate the posterior distributions of w_{dopa}, determining the probability of specific dopaminergic tone levels given the observed empirical features.

In particular, to estimate the posterior distributions of the parameter of interest, we applied SBI for efficient Bayesian model inversion. This approach was necessary because the calculation of the likelihood function at the whole-brain scale is often intractable, which makes Markov chain Monte Carlo (MCMC) inapplicable for non-parametric sampling. Note that, in the Bayesian setup, the generative model is represented by the joint distribution of model parameters and data, presenting computational and convergence challenges arising from the high dimensionality of data space despite the low-dimensionality of the parameter space. By harnessing the complexity of mechanistic models and using low-dimensional data features, SBI allowed us to efficiently infer the underlying dopaminergic tone from the observed data, providing a robust and neurophysiologically grounded understanding of the system. By using state-of-the-art probabilistic machine-learning tools for probability density estimation , such as MAF, the SBI is efficient as it relies only on forward model simulations. Moreover, since SBI requires low-dimensional data features for training the ATM and functional connectivity (FC) proved useful in this sense since it is sufficiently informative about the whole brain dynamics and captures the changes induced by the dopaminergic stimulations (as validated by the use of synthetic data). Indeed, it was observed that for each patient, the difference was evident when the summary statistics of these features applied to the ON state versus the OFF state.
Our findings indicated that Parkinson's Disease patients in the off-medication state exhibited a reduced dopaminergic tone compared to those in the on-medication state. Leveraging these estimates, we can predict individual clinical impairment, as these calculations enable us to reconstruct the clinical scenarios of patients using only their EEG signals. However, these results are to be regarded as explorative.

The effectiveness of SBI is confirmed by the close alignment of predicted and empirical data features, with the model showing particular sensitivity to changes in dopaminergic tone, capturing a general mechanism, and linking the effect of medical treatment to whole-brain dynamics, which applies to each participant. As confirmation of reliable inversion, we calculated the shrinkage to quantify the level of information in the posterior, updated from the prior. By comparing the shrinkage of the "on" and "off" states, we can assess the consistency and reliability of the distributions[39]. This means that the process allows us to replicate in silico (personalized) large-scale dynamics, predicting the effects of medical treatment on the large-scale dynamics of each patient.

Finally, we used the model to evaluate several features that were not included in the model inversion, given the inferred w_{dopa} in the ON and the OFF state. For instance, we computed the correlation between the synthetic "on-off" state differences and the empirical "on-off" differences. Notably, we observed a significant correlation between the differences, indicating that the simulated dynamics captures multiple effects of the dopaminergic tone over the large-scale dynamics.

Additionally, by examining the temporal evolution of the distribution of dopamine concentration specifically introduced in this model, we obtained further confirmation of the validity of our approach. This is evident as we observe distinct values when the starting point is 'on' compared to 'off'. While this prediction cannot be checked with the data at hand, our model predicts that patients with lower w_{dopa} will converge to a lower concentrations of Dopa in the Substantia Nigra over time, as opposed to patients with higher w_{dopa}, which will steadily display

more L_Dopa. The differences, however, are patient specific and mediated by network effects. In other words, our model predicts the ability of the nigrostriatal pathway to affect the whole-brain dynamics, which causes the whole system to stabilize in a state where less dopamine is depleted, maintaining higher bioavailability. These theoretical predictions, however, cannot be directly tested in the empirical data, as these experiments are prohibitively difficult or impossible to perform. This is the advantage of virtual brain modeling that allows us to test our hypotheses in silico by predicting the (personalized) large-scale dynamics, de facto the effects of medical treatment on the large-scale dynamics of each patient.

Future advancements might involve setting heterogeneous *w*_dopa values for each hemisphere, enhancing the representation of dopaminergic tone variability across the brain. This strategy could refine clinical interventions, facilitate comparative studies across brain hemispheres, aid in developing new biomarkers, and improve simulation models[40]. Importantly, it could enhance research into Parkinson's Disease by allowing for personalized treatment strategies. This is because accurately estimating the dopaminergic tone based on EEG data dynamics can help predict a patient's clinical state[9]. On the one hand, more biological details might be added to the model. On the other hand, more parameters might generate degeneracy and make causal estimation more challenging. Finally, further study should specifically address the problem of dyskinesias or uncontrolled involuntary movements.

Our work is complementary to most of the current modeling literature in PD, which primarily focuses on the simulation of activities in the beta range [41,42], since we focus on aperiodic activities, which have only received limited attention in Parkinson's disease thus far. Furthermore, we focus on large-scale dynamics and efficient parameter estimation with the associated uncertainty, rather than directly applying a simple optimization method[43,44].

Other modeling works in PD used mean-field models, for example in the case of the virtual Deep brain stimulation, where a multi-scale simulation approach was chosen to simulate the effects of deep brain stimulation [45,46]. However, the scope of our model is different, as we provide an explicit account of the dopamine concentration, which allows our model to tackle more closely the pathophysiological mechanisms[47]. In other words, our model explicitly incapsulates physiological knowledge about the functioning of dopamine and its effects on neural activities. Thus, the degeneration of Dopaminergic projections, a key pathophysiological feature in PD, has largely been disregared in large-scale models. Furthermore, we focus on aperiodic activities, which have not been exploited to inform synthetic models this far. Finally, our model aims at capturing the whole brain, unlike some works that modeled the basal ganglia which represent the whole cortex as a single node. In conclusion, our work analyzes EEG/LFP data from PD patients in the ON and the OFF states focusing on the aperiodic bursts, and leverages a newly designed mechanistic model that explicitly includes dopamine dynamics and differentiates the nature of the structural tracts. When tested against the ground truth (i.e. the acquisitions being performed either before or after the intake of L-Dopa), the models infer the true dopaminergic tone in all patients.

Materials and methods

Participants, EEG Data acquisition and processing

We collected resting-state data from 10 patients with Parkinson's disease, monitored both on and off levodopa medication[9]. Each session was 2 minutes long, employing deep stimulation electrodes and EEG electrodes strategically placed in the motor areas on both sides. This setup enabled simultaneous recordings from both the subthalamic nuclei (STN) and the motor cortex. Specifically, the data includes time series from 14 channels: eight local field potential (LFP) contacts (L1, L2, L3, L4, R1, R2, R3, R4) that map to the left and right STN complemented by six EEG channels (F3, Fz, F4, C3, C4, Cz).
Signal preprocessing was performed using the Fieldtrip toolbox[48]. The continuous EEG signal was first high-pass filtered at 1.3 Hz with a Hamming window, using a 'two-pass' direction, and a Butterworth filter type. Subsequently, it was down-sampled to 512 Hz and epoched into 4-second epochs. The signal underwent visual inspection to remove noisy epochs[49].

Tractography data

Minimally preprocessed diffusion and structural MRI data from 10 subjects of the human connectome project[50,51] was used to calculate the structural connectomes. The diffusion imaging data was processed with the MRtrix3 toolbox[52]. Multi-shell multi-tissue constrained spherical deconvolution with group averaged response functionn[53] was used to estimate fiber orientation distributions per voxel. After intensity inhomogeneity correction[54] , we used probabilistic tractography with anatomical constraint[55] to generate 5 million tracts per subject. Tracts were weighed using the SIFT2 algorithm[56]. We used the multimodal registration method as implemented in the Lead DBS toolbox[57] to transform the subcortical structures (GPe, GPi, STN and RN) of the DISTAL atlas[58] into the subject space. The subcortical regions together with the cortical Desikan parcellation[59] served as the mask to group weighted tracts and create the structural connectome. To compute the lead field matrix we processed the MNI152 template head with the Freesurfer recon-all[60] pipeline to obtain the cortical, as well as the 3 boundary element model (BEM) surfaces (inner skull, outer skull, and outer skin surface). We used the MNE toolbox[61] to fit a standard 10-20 EEG cap onto the skin surface of the MNI152 template head by manually setting the fiducial points (right and left pre- auricular point and nasion). Vertices of the cortical surface were used as neural electric dipoles. Together with the EEG locations and the BEM surfaces we computed the electric forward problem using the OpenMEEG toolbox[62].

Dody model for whole brain simulation

In our study, we employ *Dody model* introduced here[10] for the first time. Initially implemented to simulate the dynamics of a single node, it has been extended to simulate the whole brain activity. The model is based on neural masses designed from the adaptive quadratic integrate-and-fire model, thence incorporating neuromodulatory dynamics into its differential equations. To simulate dopamine dynamics, which is relevant in the context of Parkinson's disease, the equation 6, constituted of two terms, the first corresponding to the afferent dopaminergic input and the second to the reuptake mechanisms described with Michaelis-Menten formalism is added to the system, as:

$$\frac{dr}{dt} = 2arV + br - g_a S_a r - g_g S_g r + \frac{a\Delta}{\pi}$$

$$\frac{dV}{dt} = aV^2 + bV + c + \eta - \frac{\pi^2 r^2}{a} + (A_{Dp}[D_p]_e + B_{Dp})\, g_a S_a (E_a - V) + g_g S_g (E_g - V) - u + I_{ext}$$

$$\frac{du}{dt} = \alpha(\beta V - u) + u_d r$$

$$\frac{dS_a}{dt} = \frac{-S_a}{\tau_{S_a}} + S_{ja} c_{exc} + J_a r$$

$$\frac{dS_g}{dt} = \frac{-S_g}{\tau_{S_g}} + S_{jg} c_{inh}$$

$$\frac{d[D_p]_e}{dt} = k c_{dopa} - \frac{V_{max}[D_p]_e}{(K_m + [D_p]_e)}$$

We focus our attention on the terms c_{exc}, c_{inh}, and c_{dopa}, which are involved in the equations (4), (5) and (6), respectively. The connection-specific terms c_{exc}, c_{inh}, c_{dopa} are informed by anatomical data from scientific literature, as per understanding each brain connection as either excitatory, inhibitory or dopaminergic, and modulated by a parameter g_* through the following relations:

$$c_{exc,i} = w_{exc} \sum_i g_{exc;i,j} r_i$$

$$c_{inh,i} = w_{inh} \sum_i g_{inh;i,j} r_i$$

$$c_{dopa,i} = w_{dopa} \sum_i g_{dopa;i,j} r_i$$

where g is given by the connectome weights. In particular,cortical connections have been considered as excitatory. The cortex - basal ganglia - thalamic loop has been modelled taking into account the direct, indirect, and hyperdirect pathways [63], as reported in the Supplementary Material S1. The simulations were run for 10s by numerically integrating the system of equations, through the modified Heun method for stochastic differential equations[64,65]. The first second was discarded as a transient.

Data analysis

Estimation of avalanche transition matrices and data features

To explore the dynamics of brain activity, we analyze EEG data signals. Firstly, each signal amplitude is standardized using the z-score and then binarized, such that any time point exceeding a threshold of two standard deviations (|z| = 2) was marked as 1 (active), and all others as 0 (inactive) to compute avalanche transition matrices as described in this work [11,9].

During our analysis of EEG data and the estimation of neuronal transition matrices, a key focus is on evaluating the impact of levodopa medication on the features. We calculate an avalanche-specific transition matrix (ATM), where each element (i, j) represents the probability that region j is active at time t + 1, given that region i was active at time t. This relationship signifies the probability of sequential recruitment of any two regions by an avalanche. For each subject, we produce an average transition matrix by averaging edge-wise across all avalanches and then symmetrizing it. In our data analysis pipeline, we explore how avalanches propagate between different brain regions using ATMs. Specifically, we assess the ATMs under two different conditions for each patient: with levodopa medication (ON) and without it (OFF). This comparison sheds light on the dynamics of perturbations spreading between brain regions affected by different levels of dopaminergic stimulation. Comprehensive tests to validate the ATMs and computational details are reported in this previous work[9]. Simultaneously, avalanche transition matrices are calculated for synthetic data as well. Starting from the

simulations, the firing rates of individual brain regions are translated to the positions of the six considered electrodes using the lead field matrix. Since the position of the deep electrodes is not available, they have been approximated directly as the z-scored activities, without projecting it through the lead field. At the end of the procedure, 8 signals were generated. Each signal is z-scored, and then, similarly to the procedure described above, active regions are identified to calculate the ATM as with the empirical data. However, this time we do not take the absolute value of the signals.

Model inversion and dopaminergic tone parameter inference

The Bayesian approach offers a principled way for making inference, prediction, and quantifying uncertainty in the decision-making process by integrating information from anatomical, clinical, and mathematical knowledge [66]. Parameter estimation within a Bayesian framework involves quantifying and propagating uncertainty through probability distributions placed on the parameters (the prior), which are updated with information provided by the data (the likelihood) to form the posterior distribution [19,67]. However, accurate and reliable Bayesian inference from noisy brain data is challenging due to the high dimensionality of the data, the complex effects of brain networks, and the non-linearity involved in spatio-temporal brain organization. In particular, the calculation of the likelihood function is typically intractable, rendering MCMC sampling inapplicable[18]. In this case, we can treat the virtual brain models as a stochastic simulator that generates synthetic data similar to the empirical data, enabling inferences to be made without requiring access to the likelihood function[22,68].

Using this framework known as Simulation-based Inference (SBI [22,68]), the *Dody Model* is treated as a stochastic simulator, that is the generative model necessary to conduct Bayesian inference on dopaminergic tone, which is informed by anatomical data, to predict the features extracted from observed EEG data. To accomplish this, we trained a class of machine-learning generative models known as *Normalizing Flows* (NFs;[23]) to learn the relationship between low-dimensional data features and the parameters of an approximated posterior distribution. NFs are a family of generative models that convert a simple based distribution (e.g., the prior) into any complex target distribution (e.g. the posterior), where both sampling and density evaluation can be efficient and exact [69].

In more details, our objective is to establish plausible probability distributions for w_{dopa} parameter in the *DodyModel*, considering that the output distributions of our model should best explain a given set of experimental data features. Considering θ − as known parameter (1-dimensional, which represents w_{dopa}) and a collection of **n** data observations, denoted by the variable y_{expt}. The dynamical system analysis (previously conducted; see Refs) provides insight into the reasonable range of parameter values, allowing us to define initial (prior) probability distributions $p\left(w_{dopa}\right)$, as a uniform distribution truncated between [0.9, 7].

Using Bayes rule, the posterior distribution of the parameter values given the data is defined by the following equation:

$$p(\theta|y_{expt}) = \frac{p(y_{expt}|\theta)\, p(\theta)}{p(y_{expt})}$$

which $p(\theta)$ denotes the prior place on the w_{dopa}, and, the likelihood $p(\theta|y_{exp})$ is the probability of our model generating the data features y_{expt} given parameter θ, and $p(\theta|y_{exp})$ represents the posterior distribution that we aim to estimate.

In this work, we use SNPE (Sequential Neural Posterior Estimation [68]) a tool enabling efficient and flexible simulation-based inference on complex models without requiring access to likelihoods. SNPE dynamically refines the proposals, network weights, and posterior estimates to learn how model parameters are related to the observed summary statistics of the data. We ran SNPE using a single round to benefit from an amortised strategy (at the subject level), which can then be applied immediately to new data without needing to be retrained[22]. In this framework, we used Masked Autoregressive Flow (MAF[23]), which supports reversible nonlinear transformations and allows for highly expressive transformations with minimal computational cost.

To perform SNPE, three key inputs are required[68,70]:

(i) A prior distribution describing the biologically plausible values of w_dopa, which modulates the dopaminergic tone influencing the 'on' and 'off' states.

(ii) A mechanistic model that simulates the large-scale neural activity associated with a specific value of w_{dopa}.

(iii) A set of low-dimensional yet sufficiently informative data features, focusing here on the EEG recordings.

We trained the MAF using a budget of 3000 of simulations with random parameters sampled from the prior. The set of data features extracted from source reconstructed EEG includes summary statistics of EEG signals and of Avalanches Transition Matrices (ATM), such as kurtosis of each signal, and the functional connectivity and , from the ATMs the sum, arithmetic mean, skewness, kurtosis, the Coefficient of Variation, defined as the ratio of the standard deviation to the mean, and its inverse, the Frobenius norm and the entropy (H) of the matrix, defined as $H=-\sum(p\log2(p))$, where $\log2(p)$ is the base-2 logarithm of the probability distribution of signals. After training is complete, the posterior distribution for new observations or empirical data can be swiftly evaluated by performing a forward pass in the trained MAF. Notably, this process does not require the model or the data features to be differentiable.

Each model simulation and posterior sampling took around 60 seconds and around 30 seconds, respectively. All the steps were performed in a Workstation DELL Precision 7820 Tower with 2 Intel Xeon Silver 4214R. To run SNPE we used the public *sbi* toolbox[71].

Before running SNPE on the empirical data, we first validated the approach using synthetic data generated with known ground truth values of dopaminergic tone, and with subject-specific structural connectomes to ascertain the accuracy of the w_{dopa} estimations (see Fig 5). The plot of z-score versus posterior shrinkage for the estimated posterior, indicated an ideal Bayesian estimation for different values of w_{dopa}.

Data features

To run SBI, we identify specific data features derived from synthetic EEG data, as follows: The sum and arithmetic mean the ATM; The exponential of Skewness and Kurtosis (evaluating the asymmetry and tailedness of the ATM distribution around its mean value). The coefficient of Variation and its Inverse, which are defined as the ratio of the standard deviation to the mean, providing a normalized measure of dispersion for the ATM elements. The Frobenius norm derives a scalar magnitude of the ATM. The Shannon entropy of the ATM computing as $H=-\sum(p\ \log2(p))$, where $\log2(p)$ is the base-2 logarithm of the probability distribution of signals. We have also calculated the averaged kurtosis across each brain region and the mean value of correlation matrix between each pair (see Fig. 3 and S2).

to the training phase, the data features were smoothed using a moving average with a window size of 120 sec (see the supplementary figure xx). Subsequently, a linear regression was performed to obtain the value of the feature for each w_dopa.

Evaluation of posterior fit

To evaluate the accuracy and reliability of the Bayesian inference using synthetic data, we compute the posterior z-score (denoted by z), against the posterior shrinkage (denoted by s):

$$z = |\tilde{w}_{dopa} - w^{*}_{dopa}| / \sigma_{post};$$

$$s = 1 - \frac{\sigma^2_{post}}{\sigma^2_{prior}},$$

where the z-score is defined as the absolute value of the difference between the estimated and true values of the parameters of interest ($\tilde{w}_{dopa}, w^{*}_{dopa}$ respectively) divided by the standard deviations of the posterior, and the posterior shrinkage is given by 1 minus the ratio of the variance of the posterior to the variance of the prior.

The z-score measures how much the posterior distribution is centered around the true value, whereas the shrinkage quantifies the reduction of uncertainty over the estimate around the true value of the posterior distribution with respect to the initial prior distribution. Ideally, the distribution of posteriors derived from prior predictive observations should converge towards small z-scores and large posterior shrinkages for each parameter component. By plotting the posterior z-score (y-axis) against the posterior shrinkage (x-axis), a concentration towards the lower right suggests an ideal Bayesian estimation[19,72].

Acknowledgements

The work was supported by the European Union's Horizon 2020 research and innovation program under grant agreement No. 101147319 (EBRAINS 2.0 Project) and No. 101137289 (Virtual Brain Twin Project) and by the EBRAINS Italy nodo Italiano grant, CUP B51E22000150006.

Bibliography

1. Ascherio, A., and Schwarzschild, M.A. (2016). The epidemiology of Parkinson's disease: risk factors and prevention. Lancet Neurol. *15*, 1257–1272. https://doi.org/10.1016/S1474-4422(16)30230-7.
2. Dauer, W., and Przedborski, S. (2003). Parkinson's Disease: Mechanisms and Models. Neuron *39*, 889–909. https://doi.org/10.1016/S0896-6273(03)00568-3.
3. Horn, A., Reich, M., Vorwerk, J., Li, N., Wenzel, G., Fang, Q., Schmitz-Hübsch, T., Nickl, R., Kupsch, A., Volkmann, J., et al. (2017). Connectivity Predicts Deep Brain Stimulation Outcome in Parkinson Disease. Ann. Neurol. *82*, 67–78. https://doi.org/10.1002/ana.24974.
4. Merk, T., Peterson, V., Lipski, W.J., Blankertz, B., Turner, R.S., Li, N., Horn, A., Richardson, R.M., and Neumann, W.-J. (2022). Electrocorticography is superior to subthalamic local field potentials for movement decoding in Parkinson's disease. eLife *11*, e75126. https://doi.org/10.7554/eLife.75126.
5. Chaudhuri, K.R., and Schapira, A.H. (2009). Non-motor symptoms of Parkinson's disease: dopaminergic pathophysiology and treatment. Lancet Neurol. *8*, 464–474. https://doi.org/10.1016/S1474-4422(09)70068-7.
6. Tessitore, A., Cirillo, M., and De Micco, R. Functional Connectivity Signatures of Parkinson's Disease. J. Park. Dis. *9*, 637–652. https://doi.org/10.3233/JPD-191592.
7. Filippi, M., Sarasso, E., and Agosta, F. (2019). Resting-state Functional MRI in Parkinsonian Syndromes. Mov. Disord. Clin. Pract. *6*, 104–117. https://doi.org/10.1002/mdc3.12730.
8. Sorrentino, P., Rucco, R., Baselice, F., De Micco, R., Tessitore, A., Hillebrand, A., Mandolesi, L., Breakspear, M., Gollo, L.L., and Sorrentino, G. (2021). Flexible brain dynamics underpins complex behaviours as observed in Parkinson's disease. Sci. Rep. *11*, 4051. https://doi.org/10.1038/s41598-021-83425-4.
9. Agouram, H., Neri, M., Angiolelli, M., Depannemaecker, D., Bahuguna, J., Schwey, A., Régis, J., Carron, R., Eusebio, A., Malfait, N., et al. (2024). L-Dopa induced changes in aperiodic bursts dynamics relate to individual clinical improvement in Parkinson's disease. Preprint at medRxiv, https://doi.org/10.1101/2024.06.14.24308683 https://doi.org/10.1101/2024.06.14.24308683.
10. Depannemaecker, D., Duprat, C., Angiolelli, M., Carbonell, C.S., Wang, H., Petkoski, S., Sorrentino, P., Sheheitli, H., and Jirsa, V. (2024). A neural mass model with neuromodulation. Preprint at bioRxiv, https://doi.org/10.1101/2024.06.23.600260 https://doi.org/10.1101/2024.06.23.600260.
11. Sorrentino, P., Seguin, C., Rucco, R., Liparoti, M., Troisi Lopez, E., Bonavita, S., Quarantelli, M., Sorrentino, G., Jirsa, V., and Zalesky, A. (2021). The structural connectome constrains fast brain dynamics. eLife *10*, e67400. https://doi.org/10.7554/eLife.67400.
12. Duma, G.M., Danieli, A., Mento, G., Vitale, V., Opipari, R.S., Jirsa, V., Bonanni, P., and Sorrentino, P. (2023). Altered spreading of neuronal avalanches in temporal lobe epilepsy relates to cognitive performance: A resting-state hdEEG study. Epilepsia *64*, 1278–1288. https://doi.org/10.1111/epi.17551.
13. Romano, A., Troisi Lopez, E., Cipriano, L., Liparoti, M., Minino, R., Polverino, A., Cavaliere, C., Aiello, M., Granata, C., Sorrentino, G., et al. (2023). Topological changes of fast large-scale brain dynamics in mild cognitive impairment predict early memory impairment: a resting-state, source reconstructed, magnetoencephalography study. Neurobiol. Aging *132*, 36–46. https://doi.org/10.1016/j.neurobiolaging.2023.08.003.
14. Corsi, M.-C., Sorrentino, P., Schwartz, D., George, N., Gollo, L.L., Chevallier, S., Hugueville, L., Kahn, A.E., Dupont, S., Bassett, D.S., et al. (2024). Measuring neuronal avalanches to inform brain-computer interfaces. iScience *27*, 108734. https://doi.org/10.1016/j.isci.2023.108734.
15. Johnson, K.A., and Goody, R.S. (2011). The Original Michaelis Constant: Translation of the 1913 Michaelis–Menten Paper. Biochemistry *50*, 8264–8269. https://doi.org/10.1021/bi201284u.

16. Kringelbach, M.L., Cruzat, J., Cabral, J., Knudsen, G.M., Carhart-Harris, R., Whybrow, P.C., Logothetis, N.K., and Deco, G. (2020). Dynamic coupling of whole-brain neuronal and neurotransmitter systems. Proc. Natl. Acad. Sci. U. S. A. *117*, 9566–9576. https://doi.org/10.1073/pnas.1921475117.
17. Bullmore, E., and Sporns, O. (2009). Complex brain networks: graph theoretical analysis of structural and functional systems. Nat. Rev. Neurosci. *10*, 186–198. https://doi.org/10.1038/nrn2575.
18. Cranmer, K., Brehmer, J., and Louppe, G. (2020). The frontier of simulation-based inference. Proc. Natl. Acad. Sci. *117*, 30055–30062. https://doi.org/10.1073/pnas.1912789117.
19. Hashemi, M., Vattikonda, A.N., Sip, V., Guye, M., Bartolomei, F., Woodman, M.M., and Jirsa, V.K. (2020). The Bayesian Virtual Epileptic Patient: A probabilistic framework designed to infer the spatial map of epileptogenicity in a personalized large-scale brain model of epilepsy spread. NeuroImage *217*, 116839. https://doi.org/10.1016/j.neuroimage.2020.116839.
20. Papamakarios, G., Pavlakou, T., and Murray, I. (2017). Masked Autoregressive Flow for Density Estimation. In Advances in Neural Information Processing Systems (Curran Associates, Inc.).
21. Tejero-Cantero, A., Boelts, J., Deistler, M., Lueckmann, J.-M., Durkan, C., Gonçalves, P.J., Greenberg, D.S., and Macke, J.H. (2020). sbi: A toolkit for simulation-based inference. J. Open Source Softw. *5*, 2505. https://doi.org/10.21105/joss.02505.
22. Hashemi, M., Vattikonda, A.N., Jha, J., Sip, V., Woodman, M.M., Bartolomei, F., and Jirsa, V.K. (2023). Amortized Bayesian inference on generative dynamical network models of epilepsy using deep neural density estimators. Neural Netw. *163*, 178–194. https://doi.org/10.1016/j.neunet.2023.03.040.
23. Papamakarios, G., Pavlakou, T., and Murray, I. (2017). Masked Autoregressive Flow for Density Estimation. In Advances in Neural Information Processing Systems (Curran Associates, Inc.).
24. Gonçalves, P.J., Lueckmann, J.-M., Deistler, M., Nonnenmacher, M., Öcal, K., Bassetto, G., Chintaluri, C., Podlaski, W.F., Haddad, S.A., Vogels, T.P., et al. (2020). Training deep neural density estimators to identify mechanistic models of neural dynamics. eLife *9*, e56261. https://doi.org/10.7554/eLife.56261.
25. Ross, L.N., and Bassett, D.S. (2024). Causation in neuroscience: keeping mechanism meaningful. Nat. Rev. Neurosci. *25*, 81–90. https://doi.org/10.1038/s41583-023-00778-7.
26. Chen, L., and Campbell, S.A. (2022). Exact mean-field models for spiking neural networks with adaptation. Preprint at arXiv, https://doi.org/10.48550/arXiv.2203.08341 https://doi.org/10.48550/arXiv.2203.08341.
27. Braun, U., Schaefer, A., Betzel, R.F., Tost, H., Meyer-Lindenberg, A., and Bassett, D.S. (2018). From Maps to Multi-dimensional Network Mechanisms of Mental Disorders. Neuron *97*, 14–31. https://doi.org/10.1016/j.neuron.2017.11.007.
28. Stephan, K.E., Iglesias, S., Heinzle, J., and Diaconescu, A.O. (2015). Translational Perspectives for Computational Neuroimaging. Neuron *87*, 716–732. https://doi.org/10.1016/j.neuron.2015.07.008.
29. Van Essen, D.C., and Glasser, M.F. (2016). The Human Connectome Project: Progress and Prospects. Cerebrum Dana Forum Brain Sci. *2016*, cer-10-16.
30. Braak, H., Ghebremedhin, E., Rüb, U., Bratzke, H., and Del Tredici, K. (2004). Stages in the development of Parkinson's disease-related pathology. Cell Tissue Res. *318*, 121–134. https://doi.org/10.1007/s00441-004-0956-9.
31. Wang, H.E., Triebkorn, P., Breyton, M., Dollomaja, B., Lemarechal, J.-D., Petkoski, S., Sorrentino, P., Depannemaecker, D., Hashemi, M., and Jirsa, V.K. (2024). Virtual brain twins: from basic neuroscience to clinical use. Natl. Sci. Rev. *11*, nwae079. https://doi.org/10.1093/nsr/nwae079.
32. Sorrentino, P., Troisi Lopez, E., Romano, A., Granata, C., Corsi, M.C., Sorrentino, G., and Jirsa, V. (2023). Brain fingerprint is based on the aperiodic, scale-free, neuronal activity. NeuroImage *277*, 120260. https://doi.org/10.1016/j.neuroimage.2023.120260.
33. Yu, Y., Escobar Sanabria, D., Wang, J., Hendrix, C.M., Zhang, J., Nebeck, S.D., Amundson, A.M., Busby, Z.B., Bauer, D.L., Johnson, M.D., et al. (2021). Parkinsonism Alters Beta Burst Dynamics across the Basal Ganglia–Motor Cortical Network. J.

Neurosci. *41*, 2274–2286. https://doi.org/10.1523/JNEUROSCI.1591-20.2021.
34. Tinkhauser, G., Pogosyan, A., Tan, H., Herz, D.M., Kühn, A.A., and Brown, P. (2017). Beta burst dynamics in Parkinson's disease OFF and ON dopaminergic medication. Brain J. Neurol. *140*, 2968. https://doi.org/10.1093/brain/awx252.
35. Lofredi, R., Okudzhava, L., Irmen, F., Brücke, C., Huebl, J., Krauss, J.K., Schneider, G.-H., Faust, K., Neumann, W.-J., and Kühn, A.A. (2023). Subthalamic beta bursts correlate with dopamine-dependent motor symptoms in 106 Parkinson's patients. Npj Park. Dis. *9*, 1–9. https://doi.org/10.1038/s41531-022-00443-3.
36. Pauls, K.A.M., Korsun, O., Nenonen, J., Nurminen, J., Liljeström, M., Kujala, J., Pekkonen, E., and Renvall, H. (2022). Cortical beta burst dynamics are altered in Parkinson's disease but normalized by deep brain stimulation. NeuroImage *257*, 119308. https://doi.org/10.1016/j.neuroimage.2022.119308.
37. Vinding, M.C., Tsitsi, P., Waldthaler, J., Oostenveld, R., Ingvar, M., Svenningsson, P., and Lundqvist, D. (2020). Reduction of spontaneous cortical beta bursts in Parkinson's disease is linked to symptom severity. Brain Commun. *2*, fcaa052. https://doi.org/10.1093/braincomms/fcaa052.
38. Scarpetta, S., Morisi, N., Mutti, C., Azzi, N., Trippi, I., Ciliento, R., Apicella, I., Messuti, G., Angiolelli, M., Lombardi, F., et al. (2023). Criticality of neuronal avalanches in human sleep and their relationship with sleep macro- and micro-architecture. iScience *26*, 107840. https://doi.org/10.1016/j.isci.2023.107840.
39. Betancourt, M. (2018). Calibrating Model-Based Inferences and Decisions.
40. Wang, H.E., Triebkorn, P., Breyton, M., Dollomaja, B., Lemarechal, J.-D., Petkoski, S., Sorrentino, P., Depannemaecker, D., Hashemi, M., and Jirsa, V.K. (2024). Virtual brain twins: from basic neuroscience to clinical use. Natl. Sci. Rev. *11*, nwae079. https://doi.org/10.1093/nsr/nwae079.
41. Pavlides, A., Hogan, S.J., and Bogacz, R. (2015). Computational Models Describing Possible Mechanisms for Generation of Excessive Beta Oscillations in Parkinson's Disease. PLOS Comput. Biol. *11*, e1004609. https://doi.org/10.1371/journal.pcbi.1004609.
42. Oswal, A., Cao, C., Yeh, C.-H., Neumann, W.-J., Gratwicke, J., Akram, H., Horn, A., Li, D., Zhan, S., Zhang, C., et al. (2021). Neural signatures of hyperdirect pathway activity in Parkinson's disease. Nat. Commun. *12*, 5185. https://doi.org/10.1038/s41467-021-25366-0.
43. Deco, G., Ponce-Alvarez, A., Mantini, D., Romani, G.L., Hagmann, P., and Corbetta, M. (2013). Resting-state functional connectivity emerges from structurally and dynamically shaped slow linear fluctuations. J. Neurosci. Off. J. Soc. Neurosci. *33*, 11239–11252. https://doi.org/10.1523/JNEUROSCI.1091-13.2013.
44. Kong, X., Kong, R., Orban, C., Wang, P., Zhang, S., Anderson, K., Holmes, A., Murray, J.D., Deco, G., van den Heuvel, M., et al. (2021). Sensory-motor cortices shape functional connectivity dynamics in the human brain. Nat. Commun. *12*, 6373. https://doi.org/10.1038/s41467-021-26704-y.
45. Meier, J.M., Perdikis, D., Blickensdörfer, A., Stefanovski, L., Liu, Q., Maith, O., Dinkelbach, H.Ü., Baladron, J., Hamker, F.H., and Ritter, P. (2022). Virtual deep brain stimulation: Multiscale co-simulation of a spiking basal ganglia model and a whole-brain mean-field model with The Virtual Brain. Exp. Neurol. *354*, 114111. https://doi.org/10.1016/j.expneurol.2022.114111.
46. Saenger, V.M., Kahan, J., Foltynie, T., Friston, K., Aziz, T.Z., Green, A.L., van Hartevelt, T.J., Cabral, J., Stevner, A.B.A., Fernandes, H.M., et al. (2017). Uncovering the underlying mechanisms and whole-brain dynamics of deep brain stimulation for Parkinson's disease. Sci. Rep. *7*, 9882. https://doi.org/10.1038/s41598-017-10003-y.
47. Humphries, M.D., Obeso, J.A., and Dreyer, J.K. (2018). Insights into Parkinson's disease from computational models of the basal ganglia. J. Neurol. Neurosurg. Psychiatry *89*, 1181–1188. https://doi.org/10.1136/jnnp-2017-315922.
48. Oostenveld, R., Fries, P., Maris, E., and Schoffelen, J.-M. (2011). FieldTrip: Open source software for advanced analysis of MEG, EEG, and invasive electrophysiological data. Comput. Intell. Neurosci. *2011*, 156869. https://doi.org/10.1155/2011/156869.
49. Niso, G., Krol, L.R., Combrisson, E., Dubarry, A.S., Elliott, M.A., François, C., Héjja-Brichard, Y., Herbst, S.K., Jerbi, K., Kovic, V., et al. (2022). Good scientific practice

in EEG and MEG research: Progress and perspectives. NeuroImage *257*, 119056. https://doi.org/10.1016/j.neuroimage.2022.119056.

50. Van Essen, D.C., Smith, S.M., Barch, D.M., Behrens, T.E.J., Yacoub, E., Ugurbil, K., and WU-Minn HCP Consortium (2013). The WU-Minn Human Connectome Project: an overview. NeuroImage *80*, 62–79. https://doi.org/10.1016/j.neuroimage.2013.05.041.
51. Glasser, M.F., Sotiropoulos, S.N., Wilson, J.A., Coalson, T.S., Fischl, B., Andersson, J.L., Xu, J., Jbabdi, S., Webster, M., Polimeni, J.R., et al. (2013). The minimal preprocessing pipelines for the Human Connectome Project. NeuroImage *80*, 105–124. https://doi.org/10.1016/j.neuroimage.2013.04.127.
52. Tournier, J.-D., Smith, R., Raffelt, D., Tabbara, R., Dhollander, T., Pietsch, M., Christiaens, D., Jeurissen, B., Yeh, C.-H., and Connelly, A. (2019). MRtrix3: A fast, flexible and open software framework for medical image processing and visualisation. NeuroImage *202*, 116137. https://doi.org/10.1016/j.neuroimage.2019.116137.
53. Jeurissen, B., Tournier, J.-D., Dhollander, T., Connelly, A., and Sijbers, J. (2014). Multi-tissue constrained spherical deconvolution for improved analysis of multi-shell diffusion MRI data. NeuroImage *103*, 411–426. https://doi.org/10.1016/j.neuroimage.2014.07.061.
54. Raffelt, D., Dhollander, T., Tournier, J.-D., Tabbara, R., Smith, R., Pierre, E., and Connelly, A. (2017). Bias Field Correction and Intensity Normalisation for Quantitative Analysis of Apparent Fibre Density.
55. Smith, R.E., Tournier, J.-D., Calamante, F., and Connelly, A. (2012). Anatomically-constrained tractography: Improved diffusion MRI streamlines tractography through effective use of anatomical information. NeuroImage *62*, 1924–1938. https://doi.org/10.1016/j.neuroimage.2012.06.005.
56. Smith, R.E., Tournier, J.-D., Calamante, F., and Connelly, A. (2015). SIFT2: Enabling dense quantitative assessment of brain white matter connectivity using streamlines tractography. NeuroImage *119*, 338–351. https://doi.org/10.1016/j.neuroimage.2015.06.092.
57. Horn, A., Li, N., Dembek, T.A., Kappel, A., Boulay, C., Ewert, S., Tietze, A., Husch, A., Perera, T., Neumann, W.-J., et al. (2019). Lead-DBS v2: Towards a comprehensive pipeline for deep brain stimulation imaging. NeuroImage *184*, 293–316. https://doi.org/10.1016/j.neuroimage.2018.08.068.
58. Ewert, S., Plettig, P., Li, N., Chakravarty, M.M., Collins, D.L., Herrington, T.M., Kühn, A.A., and Horn, A. (2018). Toward defining deep brain stimulation targets in MNI space: A subcortical atlas based on multimodal MRI, histology and structural connectivity. NeuroImage *170*, 271–282. https://doi.org/10.1016/j.neuroimage.2017.05.015.
59. Desikan, R.S., Ségonne, F., Fischl, B., Quinn, B.T., Dickerson, B.C., Blacker, D., Buckner, R.L., Dale, A.M., Maguire, R.P., Hyman, B.T., et al. (2006). An automated labeling system for subdividing the human cerebral cortex on MRI scans into gyral based regions of interest. NeuroImage *31*, 968–980. https://doi.org/10.1016/j.neuroimage.2006.01.021.
60. Fischl, B. (2012). FreeSurfer. NeuroImage *62*, 774–781. https://doi.org/10.1016/j.neuroimage.2012.01.021.
61. Gramfort, A., Luessi, M., Larson, E., Engemann, D.A., Strohmeier, D., Brodbeck, C., Goj, R., Jas, M., Brooks, T., Parkkonen, L., et al. (2013). MEG and EEG data analysis with MNE-Python. Front. Neurosci. *7*. https://doi.org/10.3389/fnins.2013.00267.
62. Gramfort, A., Papadopoulo, T., Olivi, E., and Clerc, M. (2010). OpenMEEG: Opensource software for quasistatic bioelectromagnetics. Biomed. Eng. Online *9*, 45. https://doi.org/10.1186/1475-925X-9-45.
63. DeLong, M.R. (1990). Primate models of movement disorders of basal ganglia origin. Trends Neurosci. *13*, 281–285. https://doi.org/10.1016/0166-2236(90)90110-v.
64. Roberts, A. (2012). Modify the Improved Euler scheme to integrate stochastic differential equations.
65. Hussain, A. (2023). Numerical Solutions of Stochastic Differential Equations by using Heun's method.
66. Gelman, A., Carlin, J.B., Stern, H.S., and Rubin, D.B. (1995). Bayesian Data Analysis (Chapman and Hall/CRC) https://doi.org/10.1201/9780429258411.
67. Bayesian statistics and modelling | Nature Reviews Methods Primers

https://www.nature.com/articles/s43586-020-00001-2.

68. Gonçalves, P.J., Lueckmann, J.-M., Deistler, M., Nonnenmacher, M., Öcal, K., Bassetto, G., Chintaluri, C., Podlaski, W.F., Haddad, S.A., Vogels, T.P., et al. (2020). Training deep neural density estimators to identify mechanistic models of neural dynamics. eLife *9*, e56261. https://doi.org/10.7554/eLife.56261.
69. Kobyzev, I., Prince, S.J.D., and Brubaker, M.A. (2021). Normalizing Flows: An Introduction and Review of Current Methods. IEEE Trans. Pattern Anal. Mach. Intell. *43*, 3964–3979. https://doi.org/10.1109/TPAMI.2020.2992934.
70. Hashemi, M., Vattikonda, A.N., Jha, J., Sip, V., Woodman, M.M., Bartolomei, F., and Jirsa, V.K. (2023). Amortized Bayesian inference on generative dynamical network models of epilepsy using deep neural density estimators. Neural Netw. *163*, 178–194. https://doi.org/10.1016/j.neunet.2023.03.040.
71. Tejero-Cantero, A., Boelts, J., Deistler, M., Lueckmann, J.-M., Durkan, C., Gonçalves, P.J., Greenberg, D.S., and Macke, J.H. (2020). SBI -- A toolkit for simulation-based inference. Preprint at arXiv.
72. Gelman, A., Vehtari, A., Simpson, D., Margossian, C.C., Carpenter, B., Yao, Y., Kennedy, L., Gabry, J., Bürkner, P.-C., and Modrák, M. (2020). Bayesian Workflow. Preprint at arXiv.

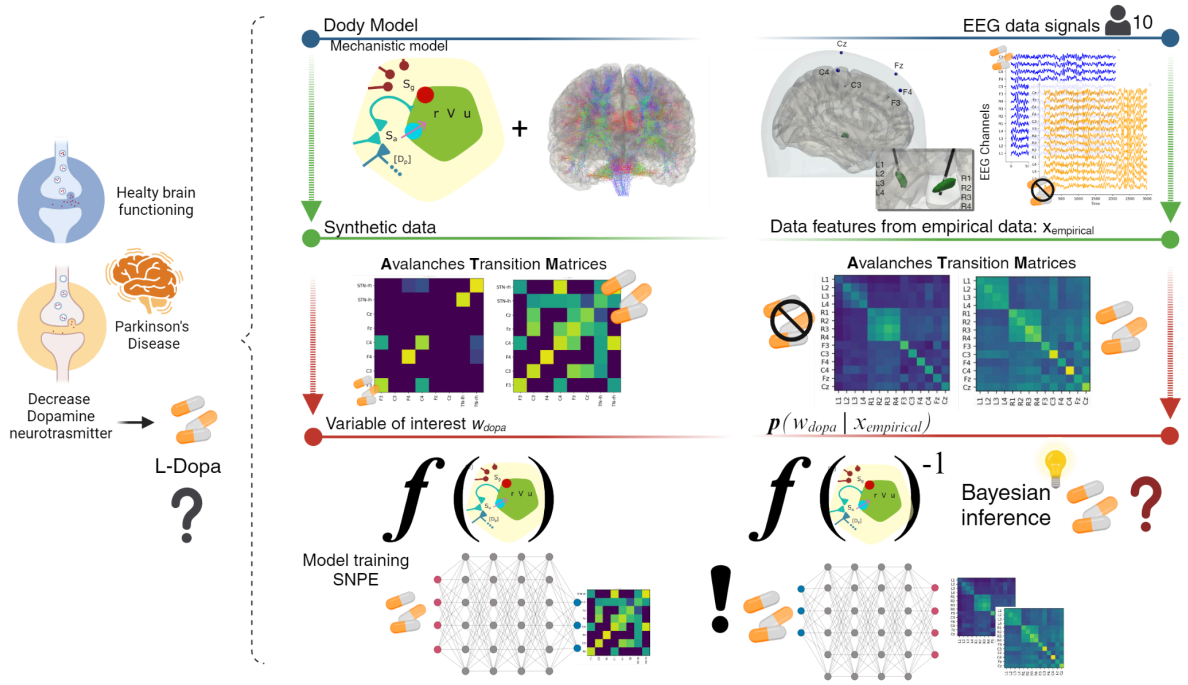

Figure 1: Overall Pipeline Summary. Parkinson's disease (PD) is characterized by a progressive decline in dopaminergic neurons and a reduction in dopamine neurotransmitter levels. dopamine is released from the presynaptic membrane to the synaptic cleft, where it binds and activates dopamine receptors on the postsynaptic membrane. Progressive degeneration of dopaminergic neurons reduces dopamine content in the SN and striatum leading to PD symptoms such as tremors, instability, slow movement, and stiffness. A common treatment involves administering L-Dopa, a drug that synthesizes dopamine, though dosing can be challenging. This study aims to explore how the nigrostriatal pathways' ability to maintain dopaminergic tone influences overall brain function. We analyzed data from EEG and deep electrodes in 10 patients with Parkinson's, recorded before and after L-Dopa administration. To model the effects of L-Dopa in silico, we developed the "Dody Model", a mechanistic neural-mass model that incorporates dopamine concentration, and Bayesian inference to infer the posterior probability distribution of dopamine concentration w_dopa given observed in the recordings. To do this, we used probabilistic machine-learning techniques (SNPE) to efficiently estimate an invertible function between parameters and low-dimensional data features. This way, we obtained a numerical prediction of the expected dynamics (in terms of properties of the ATMs), as observed in the deep electrodes and the EEG, given different dopaminergic tones.

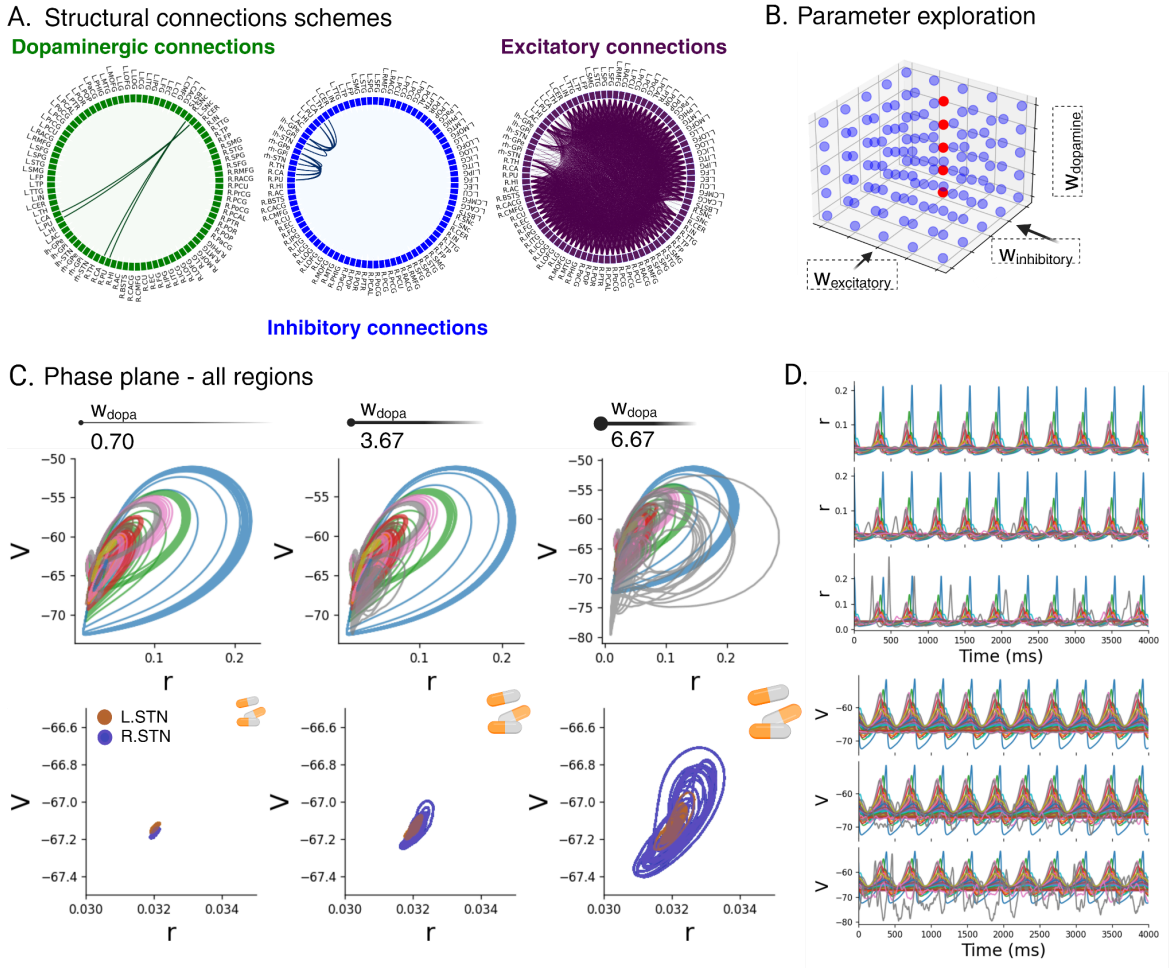

Figure 2: Dody simulation of the whole brain dynamics. Panel A shows chord diagrams representing the three types of structural connections between 88 brain regions. Connections within these layers are scaled by three factors—w_dopamine, w_inhibitory, and w_excitatory. By setting precise combinations of w_inhibitory and w_excitatory values, we show how the activity of the entire network changes (Panel B). Panel C shows the phase planes of the fast subsystem composed of the r-V variables, namely firing rate and voltage, as a function of increasing w_{dopa} (top to bottom). The corresponding time series are shown in panel D, firing rate at the top, and voltage at the bottom.

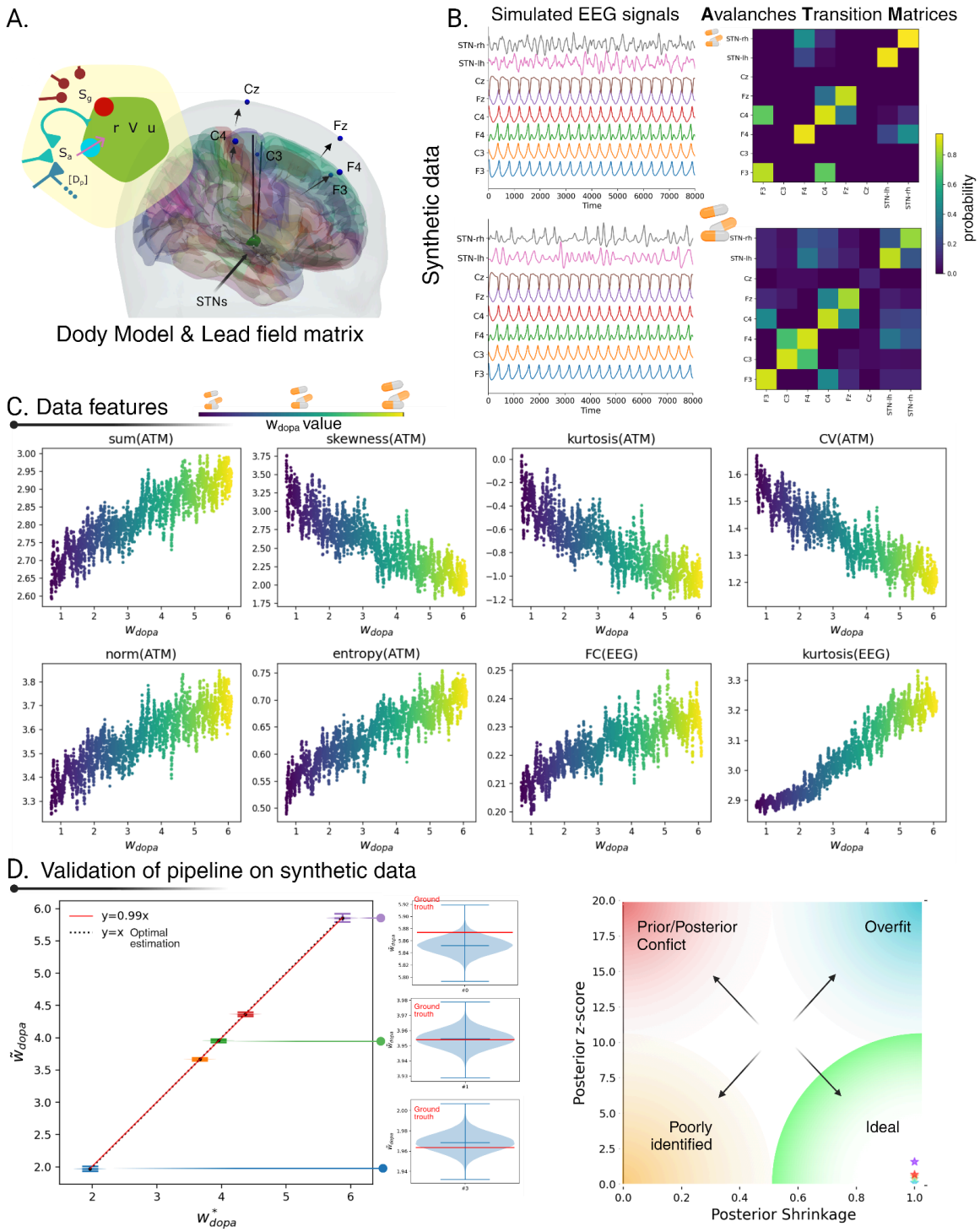

Figure 3: Analysis of simulated EEG signals and low-dimensional features extraction. The simulated data are reconstructed at the sensor level for the channels in the motor frontal area (panel A), using the lead-field matrix. Panel B details the process of feature extraction from the z-score normalized EEG synthetic data, with z=2 as threshold. Panel C shows variations of the simulated features as a function of varying w_{dopa}. The range of colors show the increase in w_{dopa} value. Panel D. illustrates the validation of SBI pipeline on 5 random synthetic datasets uniformly selected from an interval ranging from 0.9 to 6. The left plot illustrates the estimated values in black dash line, represented as \tilde w_dopa, which are interpolated by a linear regression line that closely follows the red dashed line defined by y=x, indicating a perfect fit. The right plot

displays the distribution of the posterior z-scores versus posterior shrinkage, indicating an ideal Bayesian estimation (z-scores close to zero and shrinkages close to one).

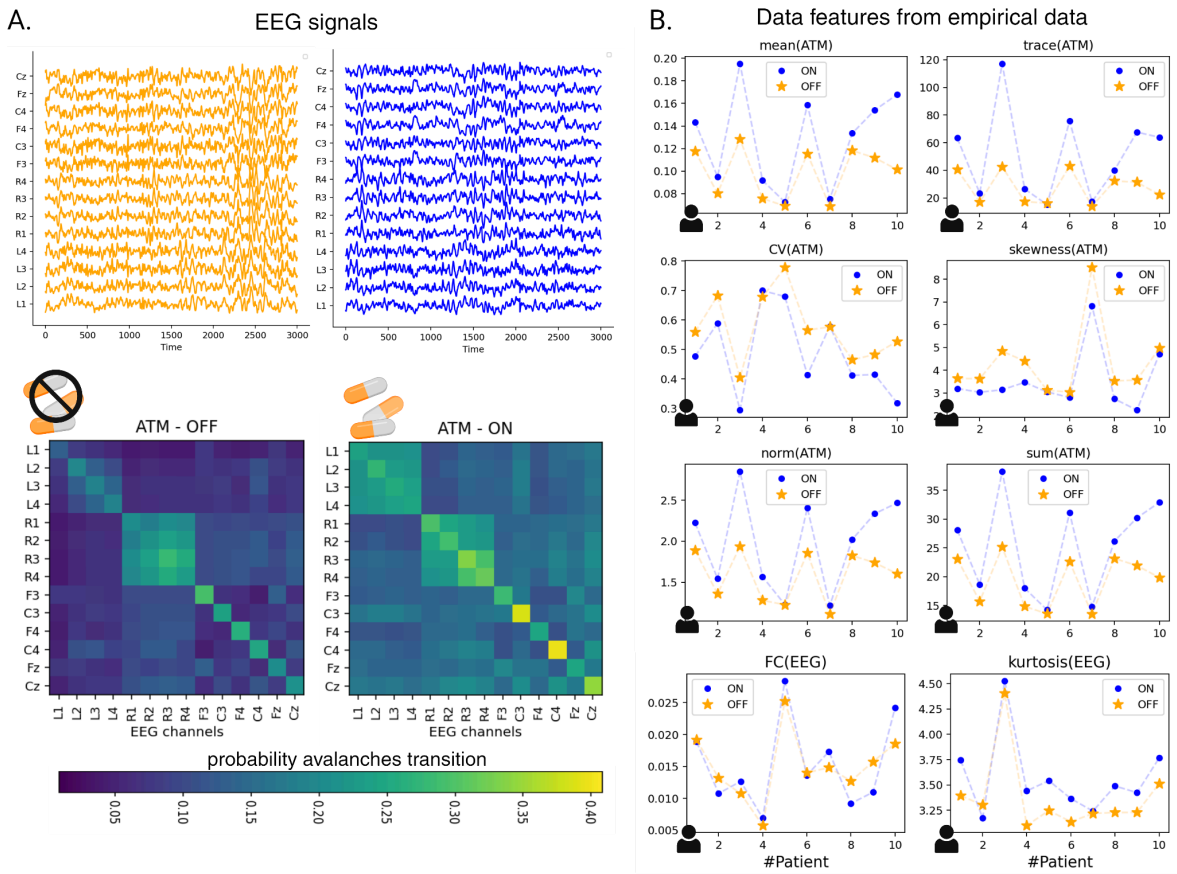

Figure 4: Data features from empirical data. Starting from the EEG signals, either acquired during the ON and the OFF state, the avalanche transition matrices (ATM) are computed (Panel A). Panel B presents a subset of the features extracted from the EEG signals and ATM matrices, for each subject in the ON (blue) and OFF (orange) states. Note that the parameters show consistent trends (wich respect to the On and the OFF states) in all the subjects.

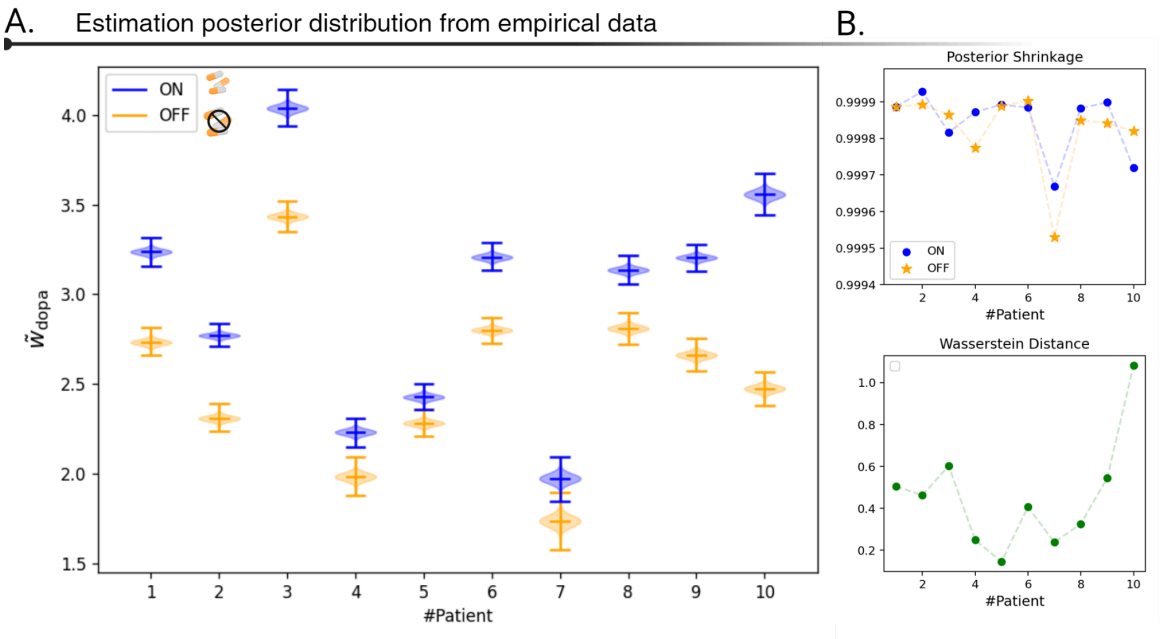

Figure 5: Bayesian estimation of w_{dopa}. Panel A shows, the estimated posterior distributions, for each patient. We can see higher values in the 'on' state compared to the 'off' state for all subjects. Panel B shows the posterior shrinkage and the Wasserstein distance to compute the uncertainty of the dopaminargic tone and the distance between the two distributions, respectively, indicating the reliability of the Bayesian estimations.

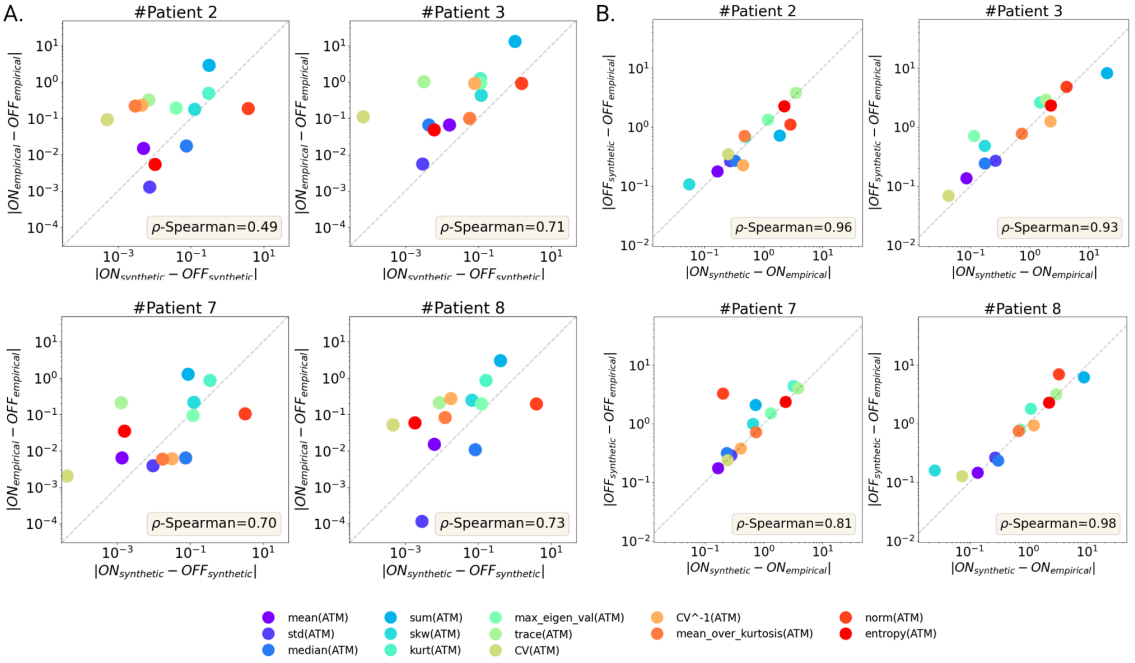

Figure 6: Comparison of the dynamics generated by the numerical simulations in either the ON or the OFF states and the corresponding observed dynamics. Panel A shows, for each patient, the Spearman's correlation between the observed and the simulated differences (average over 30 simulations) in the dynamics in the ON and OFF states across the whole set of metrics (each dot is a metric). Panel B, shows the Spearman's correlation between the difference of the features in the ON states (synthetic and simulated) and the differences for the same features in the OFF states (again, synthetic and simulated). The dashed gray line represents the equation y=x to have a guide for eyes.

Supplementary figure

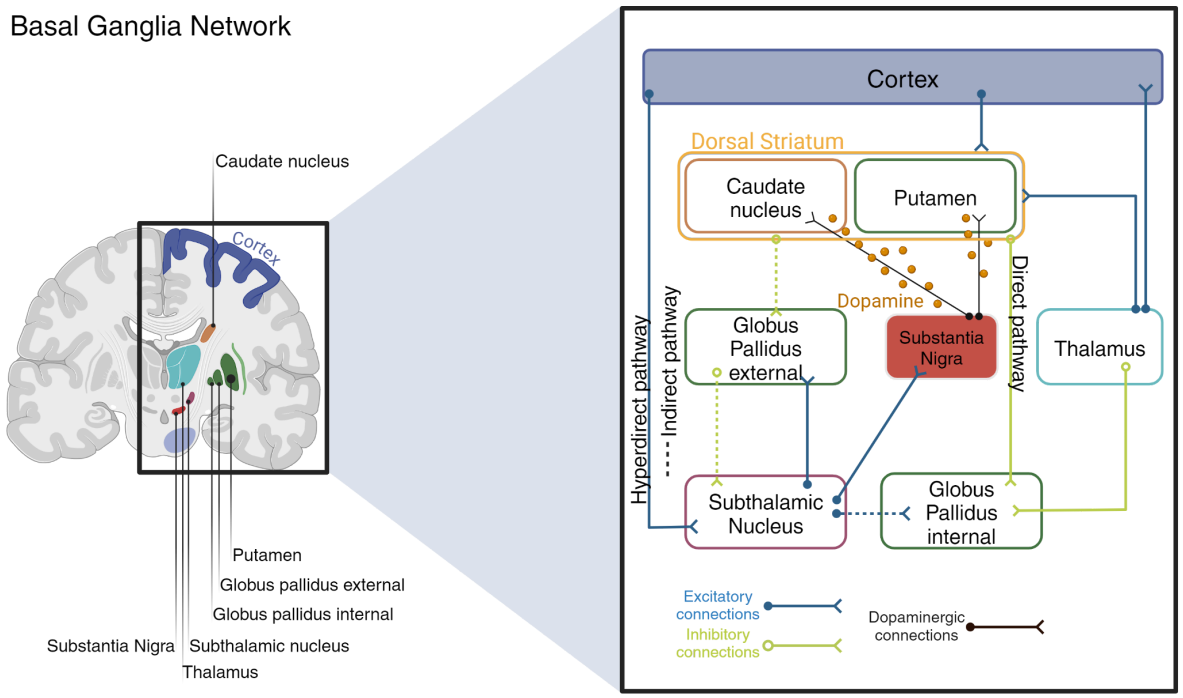

S1. Basal-ganglia neural networks. The picture shows a schematic diagram of the neural pathways in the basal ganglia. In this scheme, there are three main paths:
the Hyperdirect Pathway connecting the Cortex to the STN, the Indirect Pathway and the Direct Pathway: Excitatory connections are indicated by blue arrows while gren arrows signify inhibitory connections. The dopaminergic connections are designed in black.
Pictures created with BioRender.com

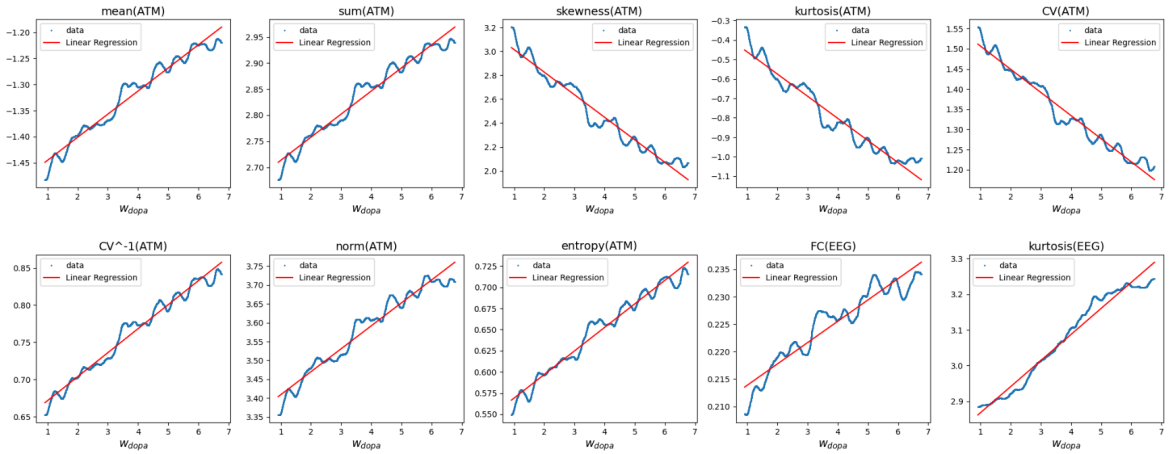

S2. Data features, linear regression model for model inversion.
This figure illustrates the data features used for training in the SBI. Instead of using the noisy values resulting from the stochasticity of the mechanistic model, they have been smoothed, and then exponential or logarithmic transformations were employed. This method was chosen to enhance the differences between the metrics in the "on" and "off" states. Additionally, the data features were projected onto a linear regression line, enabling the analysis based on their linear relationship.

The specific data features used shown include include, from top-left clockwise:
The logarithm of the mean ATM value.
The logarithm of the sum of elements of the ATM.
The exponential value of skewness.
The Frobenius norm of each ATM matrix.
The coefficient of variation of each ATM matrix.
The mean value over its standard deviation.
The Shannon entropy of the ATM matrix.
Starting from EEG signals, we also computed the functional connectivity (FC) and the kurtosis between pairs of signals.

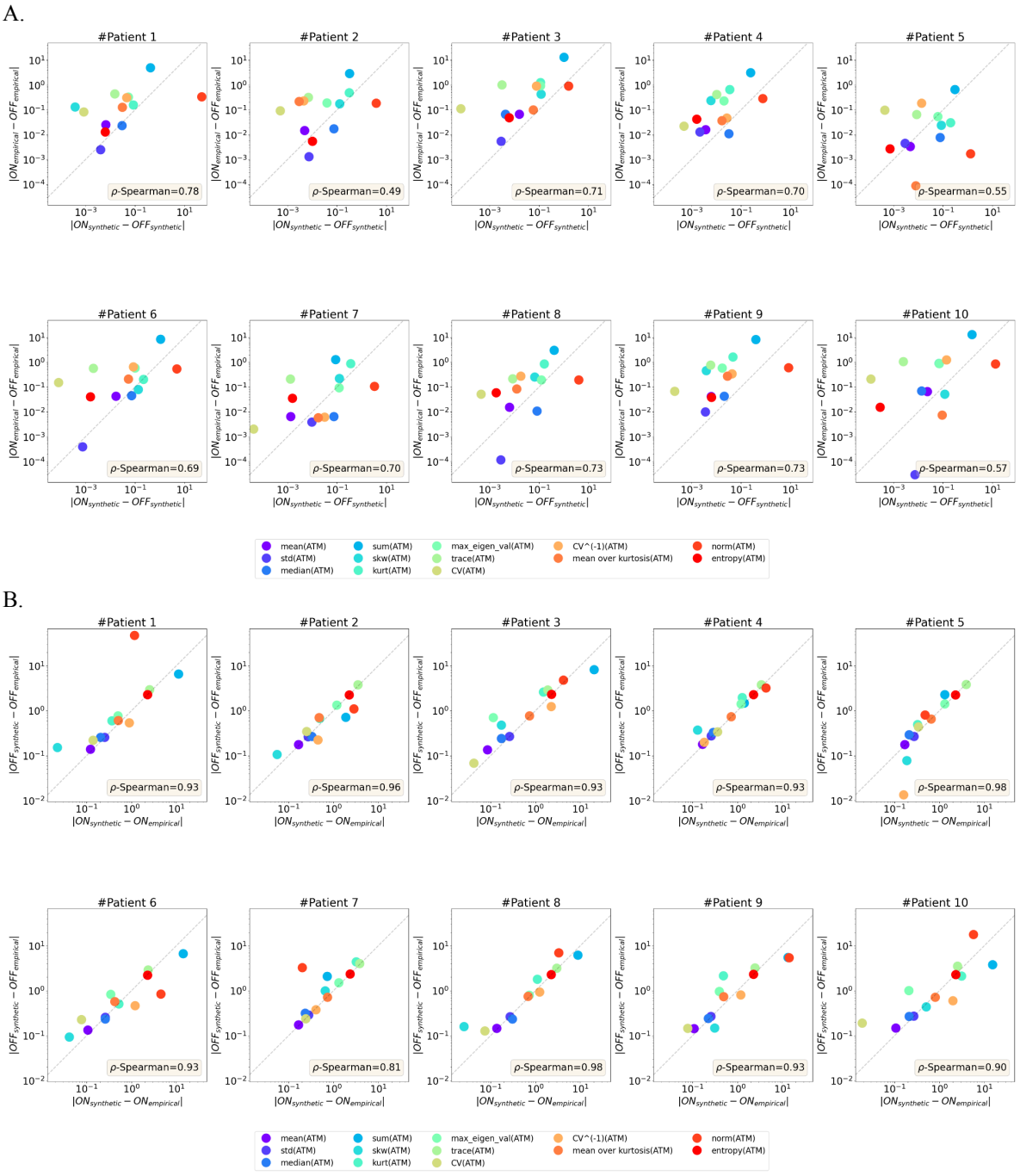

S3. Spearman's correlation between the observed and the simulated differences. Panel A, shows the simulated (y-axis) and empirical (x-axis) differences (between the ON and OFF states) across metrics. Panel B shows Spearman's correlation between the differences of the features in the ON states (synthetic and simulated, on the x axis) and the differences for the same features in the OFF states (synthetic and simulated), on the y-axis.

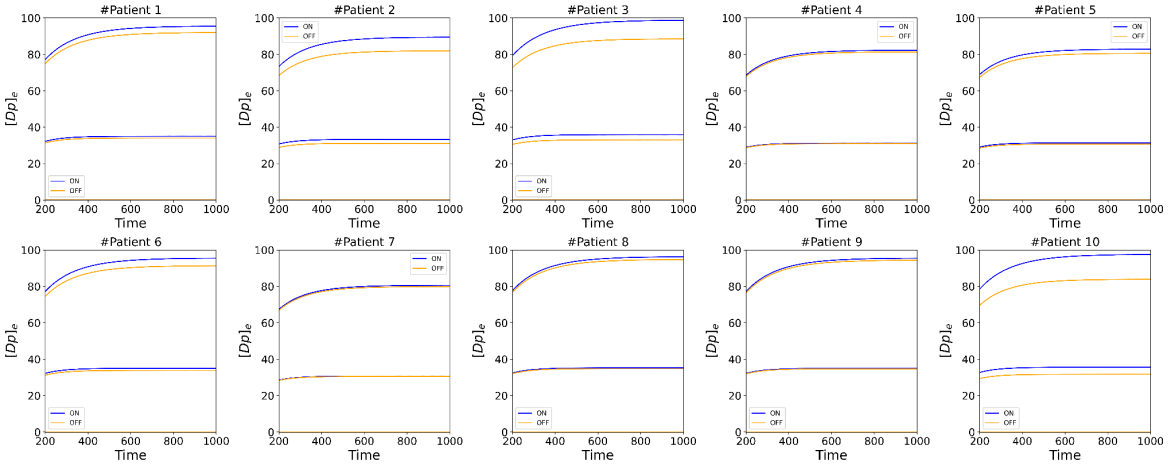

S4. Time series of the dopamine concentration in the substantia nigra during the ON (orange) and OFF (blue) state.